Supplementary information

Note 1: Transmittance simulation of the UPC-VH edge mode adapters.

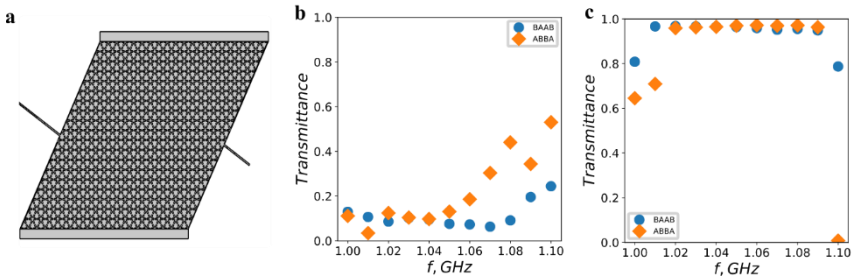

Fig. S1| Simulated transmission spectra isolating the effect of boundary engineering. **(a)** Schematic of the finite-element simulation geometry. To isolate boundary scattering effects from taper dynamics, waves are excited and received via narrow UPC waveguides of width h_0. PMLs are utilized at the longitudinal ends and transverse edges to absorb outgoing waves and simulate an open system. **(b, c)** Simulated transmittance spectra for the continuum-to-crystal adapters coupling into BA-AB and AB-BA DWs, comparing devices with (b) straight outer boundaries and (c) optimized wedge boundaries. The straight boundaries suffer massive losses due to trivial edge state excitation, whereas the optimized wedge boundaries eliminate these parasitic states to achieve near-unity transmission across a broad bandwidth.

To compare the effect of boundary engineering, the transmission spectra with straight boundaries and optimized (wedge) boundaries are simulated and compared. Instead of using the taper structure whose effect is well-known, we excite and receive phonon waves in a waveguide with a narrow width of h_0 (the width of the bridges connecting triangular sublattices). IDT is designed to excite the wave, and perfect matching layers (PMLs) are added before the IDT and at the end of receiving end to absorb transmitted power. The transmittance is defined as the ratio of output to input energy flow. Outside the outer boundaries of the PnCs is vacuum. PMLs are put at the top and bottom of the PnC to absorb energy leaking from these edges (if any reaching here) as Fig. S1shown.

To isolate the impact of macroscopic boundary engineering from the well-characterized transition dynamics of the taper structures, we performed full-wave simulations comparing the transmission spectra of devices with straight versus optimized (wedge) outer boundaries. In these simplified models, phonon waves are directly injected and extracted via UPC waveguides with a uniform narrow width of h_0 (matching the width of the interconnecting lattice bridges). IDTs are modeled as the excitation source. PMLs are applied behind the input IDT and at the receiving terminus

to absorb outgoing acoustic power and prevent artificial Fabry-Pérot reflections. The transverse outer boundaries of the PnCs are modeled as free surfaces (vacuum) to allow for the realistic excitation of trivial edge states, while additional PMLs are placed at the extreme top and bottom of the simulation domain to absorb any parasitic bulk leakage radiating from these edges (Fig. S1a). Transmittance is calculated as the ratio of the time-averaged output energy flow to the input energy flow.

The simulation results are presented in Figs. S1b-c. For PnCs featuring straight outer boundaries, both the BA-AB and AB-BA configurations exhibit severely degraded transmittance across the entire topological bandgap, with peak transmission failing to exceed 60% (Fig. S1b). This massive insertion loss computationally confirms the severe energy drain caused by the excitation of trivial edge states at the unoptimized boundaries. In stark contrast, when the modified wedge boundaries are applied—geometrically eliminating the edge terminations that support these trivial states—the transmittance recovers to a highly efficient, flat-top response of 94% to 97% spanning a broad bandwidth of over 70 MHz (Fig. S1c). We note that this idealized simulated bandwidth is wider than the experimentally observed passbands. We attribute this discrepancy to the specific fabrication constraints of the physical devices; to maintain the mechanical integrity of the suspended membrane, finite isolation trenches ($3a_0$ cuts) were utilized rather than the complete vacuum isolation modeled here, introducing minor parasitic scattering and limiting the experimental bandwidth.

Note 2: The appearance of the trivial edge state.

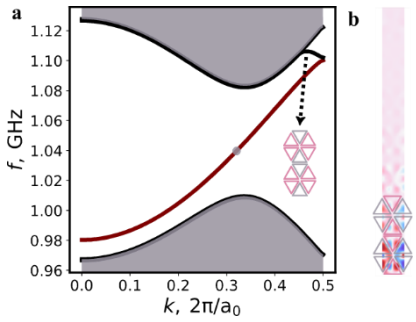

Fig. S2 | Dependence of trivial edge states on boundary termination. (a) Simulated 1D projected band structure of an AB-BA DW supercell featuring B-terminated outer boundaries, demonstrating the complete absence of trivial edge states within the topological bandgap. The inset illustrates the corresponding B-terminated supercell geometry. **(b)** Simulated spatial mode profile of a BA-AB DW supercell featuring A-terminated outer boundaries, highlighting the highly localized trivial edge state that emerges at the physical boundary.

To elucidate the physical origin of the localized states appearing at the outer PnC boundaries in Figs. 2c-d, we calculated the projected band structures for finite 1D supercells containing AB-BA and BA-AB domain walls (DWs). Notably, while a highly dispersive trivial edge state traversing the entire bandgap appears in the simulation of

the BA-AB DW supercell (Fig. 1c), no such state exists within the bandgap of the AB-BA DW supercell (Fig. S2a). By carefully examining the boundary geometries of these simulation domains, we determined that the emergence of these trivial edge states is strictly dictated by the outer lattice truncation. Specifically, the BA-AB supercell utilized in Fig. 1c features A-terminated outer boundaries (Fig. S2b), whereas the AB-BA supercell features B-terminated outer boundaries (inset of Fig. S2a).

In the fabricated devices with straight outer boundaries (Figs. 2a-b), both A-terminated and B-terminated edges inherently coexist at the inlet and outlet. Consequently, trivial edge states are excited in both the straight-boundary BA-AB (Figs. 2c, e) and AB-BA (Figs. 2d, f) configurations along their respective A-terminated edges. Because the A-terminated boundaries support these highly dispersive states across a wide frequency range, while B-terminated boundaries remain entirely free of them, parasitic energy leakage propagates asymmetrically (downward in Fig. 2e and upward in Fig. 2f). Ultimately, this confirms that unlike the topologically protected valley Hall edge modes, these trivial edge states lack topological protection and are highly sensitive to the physical termination of the macroscopic lattice.

Note 3: Analysis of the valley flipper

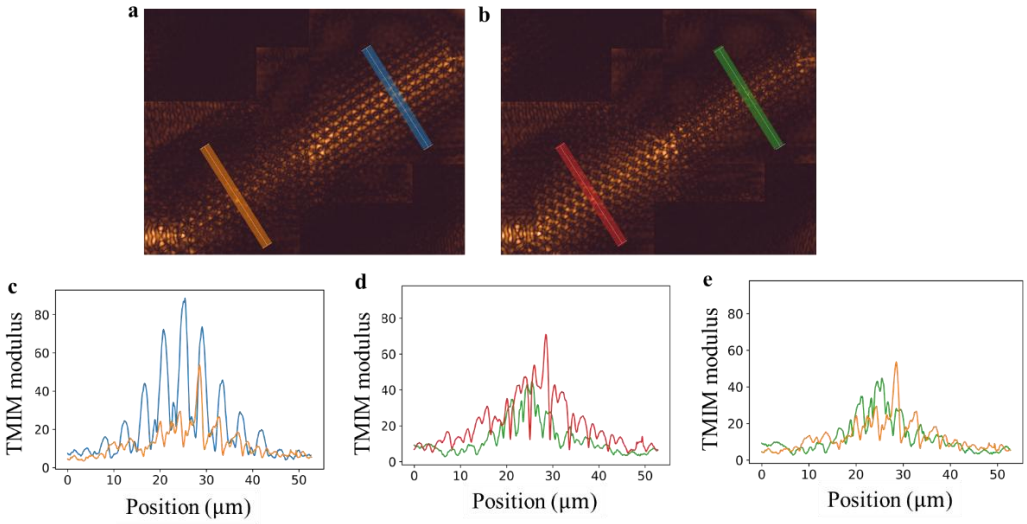

Fig. S3 | Quantitative spatial analysis of valley mixing and backscattering. **(a, b)** IFFT filtered spatial modulus maps derived from the TMIM signal, isolating the (a) K' valley and (b) K valley components propagating across the valley flipper device. The presence of minority valley components in each domain indicates backward-propagating reflections. **(c–e)** Extracted cross-sectional modulus profiles comparing the specific colored line cuts indicated in panels (a) and (b). These integrated profiles are used to calculate the relative power density ratios of the backscattered minority valleys (c, d), and the near-unity forward transmission efficiency across the central junction (e).

While the cross-sectional integration of the mode profile (Figs. 3g-h) indicates highly efficient energy transfer across the central valley-flipping junction, the raw FFT spectra simultaneously reveal the coexistence of both K and K' valley components within each domain wall. Due to the valley-momentum locking of the topological edge states—where forward and backward propagating modes at a given DW strictly occupy opposite valleys—the presence of a minority valley component in either domain acts as a direct signature of backscattering. To pinpoint the origin of this backscattering, we employed an Inverse Fast Fourier Transform (IFFT) to selectively filter and reconstruct the spatial distributions of the individual K' and K valley components (Figs. S3a and S3b). These filtered maps demonstrate spatial valley mixing: the K' valley, while predictably dominant in the AB-BA DW, also maintains a clear presence in the BA-AB DW (Fig. S3a). Conversely, a non-negligible K valley signal is observed in the AB-BA DW.

We deduce that this valley mixing is not caused by parasitic reflection at the central valley-flipping junction, but rather by reflections occurring at the device outlet (the downstream AB-BA to UPC adapter). Quantitatively, the power density ratio of the minority K' mode in the BA-AB DW to the dominant K' mode in the AB-BA DW is 0.354 (Fig. S3c). Similarly, the ratio of the minority K mode in the AB-BA DW to the dominant K mode in the BA-AB DW is 0.379 (Fig. S3d). If this ~35–38% modal fraction were lost to reflection at the central junction itself, the overall transmitted intensity in the AB-BA DW would be drastically lower than the incident intensity in the BA-AB DW. However, the total modal energy remains remarkably consistent across both domains. Specifically, comparing the integral of the filtered profiles (the orange and green lines in Figs. S3a-b) yields an energy ratio of 0.959 (Fig. S3e), while the ratio of the blue to red lines approaches unity. Therefore, we conclude that the forward-propagating mode experiences near-unity transmission across the central flipper. The minority valley components arise solely because the transmitted wave partially reflects at the downstream UPC outlet, creating a backward-propagating wave (occupying the opposite valley) that subsequently undergoes highly efficient reverse valley-flipping as it travels backward through the central junction.

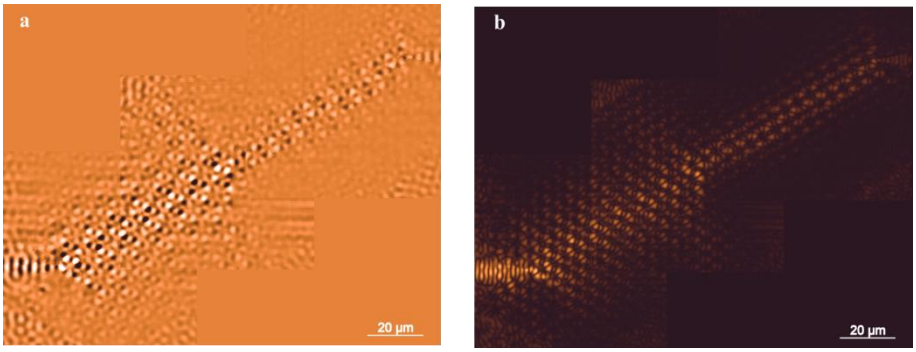

Fig. S4| Parasitic leakage at the central valley-flipping junction. (a) TMIM amplitude image of a secondary valley flipper device at 1.050 GHz, revealing distinct energy leakage from the central intersection into the diverging upper and lower BA-AB DWs. **(b)** The corresponding TMIM modulus profile mapping the

total acoustic energy across the device. The profile visually confirms the attenuation of the forward-propagating mode, resulting from the finite isolation cut length that permits evanescent coupling into the diverging topological pathways.

While the device analyzed in Fig. 3 demonstrates near-unity transmission across the central valley-flipping junction, fabrication constraints can occasionally lead to noticeable parasitic leakage. As shown in Fig. S4, significant energy leakage into the diverging upper and lower BA-AB DWs is observed in a secondary valley flipper device (Fig. S4a). This parasitic routing results in a pronounced decrease in the modulus intensity of the forward-propagating beam across the junction (Fig. S4b). We attribute this leakage to the limited length of the physical isolation cuts (restricted to approximately three lattice periods to maintain the mechanical stability of the suspended membrane). This finite isolation permits unwanted evanescent coupling across the topological four-quadrant intersection, allowing the wave to partially scatter into the orthogonal diverging pathways. This case, when contrasted with the highly efficient device in Fig. 3, highlights the sensitivity of the topological routing to the physical isolation at the central junction. Future device iterations employing optimized intrinsic film stress will enable the fabrication of suspended membranes with longer isolation trenches, which will suppress this evanescent leakage.